

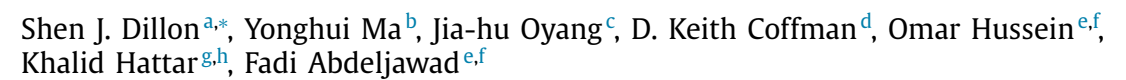
Contents lists available at ScienceDirect

Acta Materialia

journal homepage: www.elsevier.com/locate/actamat



Interface nucleation rate limited densification during sintering





- ^a Department of Materials Science and Engineering, University of California, Irvine, CA 92697, USA
- ^b Yantai Research Institute of Harbin Engineering University, Yantai, Shandong, 264006, China
- ^c School of Materials Science and Engineering, Harbin Institute of Technology, Harbin, 150001, China
- ^d Department of Materials Science and Engineering, University of Illinois Urbana-Champaign, Urbana, Illinois, 61801, USA
- e Department of Mechanical Engineering, Clemson University, Clemson, South Carolina, 29634, USA
- ^f Department of Materials Science and Engineering, Clemson University, Clemson, South Carolina, 29634, USA
- g Materials, Physical, and Chemical Sciences, Sandia National Laboratories, Albuquerque, NM 87185, USA
- ^h Department of Nuclear Engineering, University of Tennessee, Knoxville, TN, 37996, USA

ARTICLE INFO

ABSTRACT

Article history: Received 2 June 2022 Revised 9 October 2022 Accepted 17 October 2022 Available online 19 October 2022 In situ bicrystal sintering experiments performed in a transmission electron microscope indicate that the densification rate can follow interface nucleation rate limited kinetics. This work performs in situ sintering experiments on immiscible Al₂O₃-GdAlO₃ interfaces enabling a statistical treatment of sintering at a single interface type as a function of time and temperature. The data provide a measure for the activation energy of the nucleation process, ≈4.8 eV. This large value is consistent with observations that the process is rate limiting. A new sintering model is developed based on the assumption of interface nucleation rate limited kinetics and is demonstrated to work well in predicting in situ bicrystal sintering data, fitting in situ multiparticle sintering data, predicting grain size versus density sintering trajectories, and fitting isothermal bulk sintering data.

© 2022 The Authors. Published by Elsevier Ltd on behalf of Acta Materialia Inc. This is an open access article under the CC BY license (http://creativecommons.org/licenses/by/4.0/)

List of symbols	
$\dot{\varepsilon}_0$	Strain rate pre-exponent
A_g	Area of grain boundary
A_V	Surface area per volume
D_s	Surface diffusivity
H^*	Activation enthalpy
R^2	R-squared metric for fit quality
r_n	Neck radius of curvature
S*	Activation entropy
ν^*	Activation volume
v_f	Grain boundary point defect formation volume
w_s	Work done during densification specifically in the time
	interval when strain is active at a single boundary
w_T	Total work done across a period associated with densifi-
	cation at a single boundary
γs	Surface energy
$\Delta G_{s,c}$	Total change in Gibbs free energy during densification
	specifically in the time interval when strain is active at
	a single boundary

Strain rate Critical sintering stress at which strain is activated $\sigma_{s,c}$

 Σ_s Sintering potential Sintering stress σ_{s} Yield strength σ_{y}

 $\dot{\varepsilon}$

Shape factor relating $A_{V} = B_{d}$

В Average grain size d D Diameter of grain

G Gibbs free energy Boltzmann constant

Mean width \mathcal{L} Length of Grain

Perimeter of grain р Grain radius

Τ **Temperature**

Grain boundary width ΔG_T Total change in Gibbs free energy across a period associ-

ated with densification at a single boundary

Sintering strain

'Efficiency' factor describing the fraction of dissipated interfacial energy that does work on the densification process

E-mail address: sdillon1@uci.edu (S.J. Dillon).

Corresponding author.

- η 'Efficiency' term describing how much of the work done on the densification process contributes to densification
- ν Concentration of surface defects mediating diffusion
- Ξ Constant describing the slope $\frac{d\varepsilon}{d(A_{M})}$
- σ Stress
- φ Turning angle at surface triple junction
- Ω Atomic or molecular volume

1. Background

Sintering is the primary solid-state powder consolidation technique that has broad applications across a range of materials classes and technological systems [1–8]. Sintering science remains an important area of materials research as novel sintering processes and new applications continue to emerge [9,10]. Sintering, for example, provides a route to consolidate additively manufactured colloidal green bodies, that can often be prepared with better spatial resolution than melt based processes [11]. New sintering techniques introduced in recent decades have generated uncertainties regarding the fundamental mechanisms for sintering [12-16]. There, furthermore, continues to be a need to reproducibly consolidate near-net-shaped materials for demanding applications that challenge the discipline, such as dispersion strengthened nanostructured alloys for extreme environments, high density transparent ceramics for laser applications, or high-quality refractory ceramics for hypersonic vehicles [11,17,18].

GB mediated densification during sintering requires mass transport away from grain boundaries (GBs) and towards pore surfaces. The process occurs via three steps, (a) the nucleation of GB dislocations, (b) the emission and absorption of point defects at the free surface and GB dislocation, and (c) point defect fluxes between the source and sink, either through the GB or through the lattice. Any of these three processes, shown schematically in Supplementary Figure S1, could be kinetically rate limiting. These three mechanisms exhibit different driving force dependencies, (a) exponential, (b) parabolic, and (c) linear, respectively. This causes them to be dominant at different relative driving forces, depending on the underlying microstructure; see Supplementary Figure S2. Despite the low average driving force for sintering of micron and sub-micron scale particles, models typically applied to sintering, such as those developed by Coble [19] and others [20], generally assume diffusion limited kinetics that dominates at large driving forces. This inherently assumes GB dislocation nucleation and point defect emission/absorption are facile, which is inferred by an assumption that grain boundaries are ideal point defect sources and sinks. It has, however, been hypothesized that point defect emission and absorption kinetics could be rate limiting during sintering [21], although such models have primarily been applied to creep [22]. Coble predicted that such a point defect emission/absorption limited sintering model would be indistinguishable from a diffusion limited model during isothermal experiments due to scaling arguments [19], which has been confirmed by detailed analysis [23,24]. As will be shown herein, the GB dislocation nucleation rate limited kinetic model is also effectively indistinguishable from the diffusional and point defect emission/absorption limited kinetic models when analyzing isothermal data. As discussed qualitatively in a recent paper [25], however, the different mechanisms will exhibit different activation energies, influence residual stress evolution, the evolution of the pore size distribution, and respond differently to novel heating schedules during processes such as high heating rate sintering [13,15,26] or two-step sintering [27]. Thus, identifying the appropriate rate limiting process is of considerable practical importance.

Despite the lack of an analytical model for the nucleation rate limited kinetics, the idea that densification should be described in terms of GB plasticity and the importance of dislocation nucleation at and around sintering boundaries has been discussed within the literature [28,29]. GB dislocation nucleation rate limited sintering, and creep, models have not received significant attention because the stresses necessary to nucleate such defects typically far exceed average sintering stresses in powder compacts [22]. The problem has largely been ignored by assuming that sufficient GB dislocations pre-exists and somehow self-propagate or multiply [22]. Limited evidence for such phenomena exists. Alternatively, a stress concentration should be active in driving local stresses at individual boundaries to values far greater than the average sintering stress.

A possible mechanism for stress concentration was discussed by Sudre and Lange [30]. They described criteria wherein the shrinkage of a particle confined between two other particles would undergo de-sintering. De-sintering occurs when $\gamma_{GB} > 2\gamma_s$, where γ_{GB} and γ_s are the grain boundary and surface energies, respectively. This can occur when the local stress at the boundary exceeds the work of adhesion. Particle shrinkage dissipates surface energy decreasing the total energy of the system but can also locally increase the chemical potential at the GB. Thermodynamic work driven by surface energy dissipation, therefore, can drive local stress evolution to values much larger than the average sintering stress of the entire system. Similar ideas have previously been invoked to understand residual stress evolution during sintering [31]. DeHoff [32] also hypothesized that an energy dissipation model could account for the relationship between grain size and density during sintering and posited that;

$$\frac{d\varepsilon}{d\binom{A_{V}}{V}} = \Xi \tag{1}$$

where Ξ is a constant, $(^A\!/_V)$ denotes the surface area per unit volume, and ε is strain. DeHoff [32] ultimately ascribed Ξ to a topological effect, but it is hypothesized here that it primarily reflects physical properties of the GB. A relationship between these microstructural variables has indeed been noted by several authors [33,34].

A recent series of in situ transmission electron microscopy (TEM) bicrystal creep experiments performed on high index cubic ZrO₂ GBs support the notion that GB dislocation nucleation rate could play an important role in sintering [35,36]. Similar bicrystal creep and sintering experiments were performed on random interfaces between immiscible Al₂O₃ and GdAlO₃ grains [25] in order to avoid complications introduced by grain boundary migration. The schematic in Fig. 1 outlines the general response observed in these prior experiments, which forms the basis for a proposed initial stage sintering model. In general, the sintering stress increases with no associated densification strain up until a critical stress value, $\sigma_{s,c}$, followed by densification strain, at a rate consistent with diffusional models, and sintering stress relaxation. The discontinuous nature of the process indicates the GBs do not serve as ideal sinks for continuous point defect fluxes and is generally consistent with nucleation rate limited kinetics. The overall process results in a reduction in the total free energy of the system. This schematic depicts a single critical sintering stress for simplicity, but this is, in fact, a distribution defined by the activation volume, v^* , as [37]

$$v^* = -kT \left(\frac{d\ln \dot{\varepsilon}}{d\sigma}\right)_{T,\dot{\varepsilon}_0} \tag{2}$$

where $\dot{\varepsilon}$ is strain rate, σ is stress, and kT is the thermal energy in the system. These results suggest that during sintering GBs indeed sample local stress states far greater than the average sintering stress and large enough to nucleate climb mediating GB dislocations. A goal of this work is to construct and test a model based

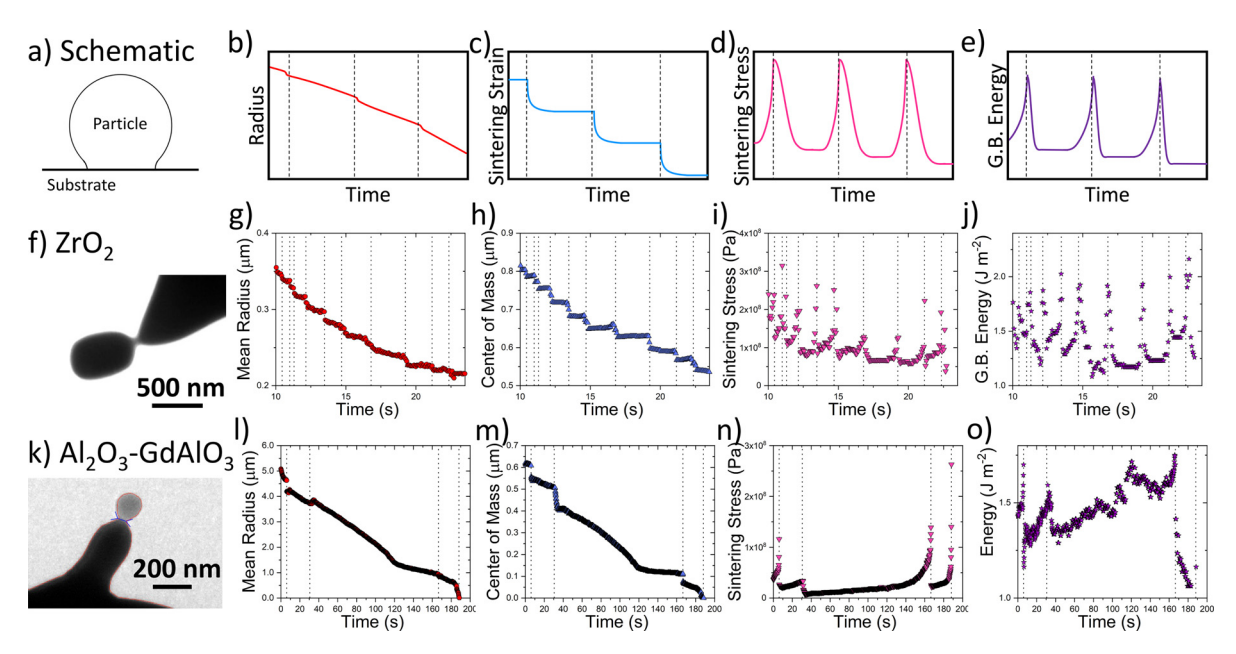


Fig. 1. Schematic representation of the variation in particle radius, sintering strain, sintering stress, and GB energy evolution during sintering, along with experimental observations of such phenomena in ZrO_2 and Al_2O_3 -GdAlO₃. The dotted lines denote points in time where densification occurs, which has a corresponding rigid body motion. At those points in time, the rate of densification is consistent with measured GB diffusivities. Note that the center of mass can vary via both densification and Ostwald ripening, but the former is discontinuous while the latter is continuous on the time scale of the observation. The measurements of strain and stress are the basis for calculating thermodynamic work associated with densification forming the basis of the model in this text.

on the hypothesis that densification is interface rate limited by the nucleation rate of climb mediating interfacial dislocations.

This effort seeks to develop an analytical nucleation rate limited kinetic model for sintering based on the primary assumption that surface energy dissipation during coarsening drives stress concentrations that facilitate GB dislocation nucleation. The model is initially validated against prior in situ bicrystal sintering and creep experiments, as well as prior molecular dynamics simulations of bicrystal sintering. The lack of prior systematic temperature dependent bicrystal sintering experiments motivate a set of model experiments focused on pearl necklace type structures composed of alternating Al₂O₃ and GdAlO₃ eutectic grains that are observed during in situ TEM sintering experiments. Eutectic structures serve as a model, because each pair of grains has the same misorientation, and aligned growth of these structures produces interfacial planes with nominally the same crystallography [38,39]. These experiments afford a temperature dependence and an approximate activation energy that provide insights into whether the proposed mechanism is reasonable. The model is also extended to fitting polycrystalline sintering data from the literature to both demonstrate the efficacy of the model in fitting such data and provide example temperature dependent trends in several systems.

2. Experimental methodology

Al $_2$ O $_3$ -GdAlO $_3$ powder was prepared at the eutectic composition using a co-precipitation process detailed elsewhere [38]. The material was consolidated using spark-plasma sintering followed by melting in a Mo crucible at 1770 °C under Ar, as discussed in a prior paper where the same samples were mechanically tested [38]. Bulk samples were polished into wedge-shaped geometries with an edge thickness on the order of \approx 10 μm . Focused ion beam (FIB, FEI Helios) milling with a final step at 30 keV Ga and 0.5 nA was utilized to prepare needle-shaped samples from portions of the eutectic where the interphase boundary aligned approximately perpendicularly with the needle axis. The process is anticipated to introduce Ga contamination <30 nm into the surface [40]. During heating, however, this material is observed to precipitate on the

surface and then evaporate. Residual Ga likely remains in the sample, but at levels closer to its equilibrium solubility.

Samples were heated within the TEM using a 1064 nm laser with an ${\approx}50~\mu m$ spot. The laser power is linear in applied power above a threshold, and it has generally been observed in this material, and others, that the specimen temperature is linear in power for a given phase. This has been determined via electrical conductivity measurements [41], lattice parameter expansion [42], and optical pyrometry. Reference temperatures provide a useful route to calibrating the temperature well. For the experiments described here, every sample was observed in situ under the conditions discussed, and then the power was raised to the melting temperature in the same region of observation. This provides a reference temperature to calibrate the linear thermal expansion against. All experiments were performed within 26% of the eutectic temperature. The temperature is typically raised slowly in increments of \approx 20–50 °C. Video data was acquired at 4-5 frames per second using Gatan Digital Micrograph. Video frames were analyzed using Image] and Matlab.

The surface energy is not known explicitly for our material and is challenging to measure for samples composed of phase boundaries, since multiple interfaces exist. For simplicity, a value of 1 J m^{-2} is assumed for calculating the sintering stress [43,44]. This value is of a reasonable magnitude for the samples investigated and the value is convenient for simply rescaling the results to alternative formulations. The model described below has γ_S in the numerator, but it also appears in the denominator in the calculated sintering stress term. Thus, any consistent value assumed will cancel when applying the sintering model. The critical sintering potential is calculated from $\Sigma_{s,c} = \gamma_S(2\pi x cos \varphi - \pi \frac{x^2}{\mathcal{L}})$, where φ is the turning angle at the triple line, x is the interface radius, $\mathcal{L} = \frac{p}{\pi - \sum_{i=1}^n \varphi}$ is the mean width where p is the perimeter of the convex hull around the particle, π takes its typical numerical value, and $\sum_{i=1}^n \varphi$ is the summation of the turning angles over each of the junctions. This is based on the treatment of sintering potential by Cannon and Carter [45], where the mean curvature in their

model is approximated by $^{1}/_{\mathcal{L}}$ here. The critical sintering stress is approximated as $\sigma_{s,c}=^{\sum_{s,c}}/_{A_g}$ where $A_g=\pi x^2$ is the area of the GB assuming a circular cross section. The circular cross-section assumption may not hold for any individual measurement but is expected to provide a reasonable measure when averaged over many observations.

Measurements were obtained from the Al₂O₃ particles since they appeared to primarily be active in terms of interfacial strain. Supplementary Figure S3 highlights the geometric features measured. This is consistent with prior observations that the Al₂O₃ portion of the phase boundary is considerably more facile than the GdAlO₃ portion of the interface. An ImageJ script was used to calculate the convex hull, the dihedral angles were measured manually, and the center of mass of grains was calculated from the threshold of the grain in ImageJ and calculated with respect to the center of the grain boundary. Finally, the model developed herein was evaluated numerically using Matlab. Specifically, the code was used to fit data using an iterative process and predict sintering trajectories based on measured materials properties.

3. Model

In this model, a sintering stress concentration evolves at the sintering neck due to dissipation of surface energy, γ_S , by reduction in its area during coarsening, which lowers the overall free energy density of the system,

$$dG = \gamma_S d\left(^A\!/_{\!V}\right) \tag{3}$$

where $(^{A}\!\!/_{\!V})$ denotes the surface area per unit volume. From the activated state, work per volume,

$$dw = \sigma_{\rm s} d\varepsilon \tag{4}$$

is done to induce densification strain, ε , at the sintering stress, σ_s . An equality between these two terms may be produced by introducing efficiency terms, ζ and η . The former describes the fraction of the dissipated surface energy that is converted into work for the overall sintering process, ΔG_s ,

$$\Delta G_{S} = \gamma_{S} \left({}^{A}_{/V} \right) \zeta \tag{5}$$

The latter efficiency term will be used to describe the work done during sintering strain (w_s) taken to be,

$$w_{S} = \sigma_{s,c} \varepsilon \eta \tag{6}$$

where $\sigma_{s,c}$ is the critical sintering stress associated with the onset of GB plasticity. Equating the differential work terms in Eqs. (3) and (4) while including the efficiency terms from Eqs. (5) and (6) produces:

$$\frac{d\varepsilon}{d\left(\frac{A_{V}}{V}\right)} = -\frac{\gamma_{S} \zeta}{\sigma_{s,c} \eta}.$$
 (7)

This relation should, in general, be true for pressureless sintering where dissipation of surface energy drives the process. If we take a compressive strain as positive, then the term on the right-hand side of Eq. (7) will be negative. The process will be interface nucleation rate limited when $\sigma_{s,c} >> \overline{\sigma_s}$, where $\overline{\sigma_s}$ is the average sintering stress. The magnitudes of $\sigma_{s,c}$, ζ and η , however, have not been known or subject of detailed investigation. $\sigma_{s,c}$ was recently measured for bicrystal sintering in ZrO₂ [35]. Fig. 2a replots data from that work in terms of $\binom{A}{V}$ versus ε . Fig. 2b shows the corresponding probability of discontinuous densification steps occurring as a function of sintering stress, where the probability is calculated based on the time spent in a specific sintering stress interval. The inverse average slope of the curve in

Fig. 2a is $\frac{d\varepsilon}{d\langle A_{V}\rangle} = -\frac{\gamma_S}{\sigma_{S,c}\eta} = 2.3 \times 10^{-8}$ m. The data in Fig. 2a indi-

cates that $\sigma_{s,c} \approx 1 \times 10^8$ Pa, assuming for now $\zeta \approx 1$ and $\eta \approx 0.5$, which is in good agreement with the more direct measurements of $\sigma_{s,c} = 1 \times 10^8 \ Pa - 2 \times 10^8 \ Pa$ shown in Fig. 2b, which was measured directly from geometric analysis of the bicrystal sintering. Fig. 2c compares this to the GB tensile yield strength measured as a function of strain rate and temperature. The strain rate during sintering at 1851 °C is on the order of 10^{-3} s⁻¹. This suggests that the yield stress measured as the deviation from the linear response during tensile loading, σ_{v} , is in reasonable agreement with the critical stress to induce densification calculated from the model and directly from imaging; $\sigma_{v} \approx \sigma_{s.c}$. These prior measurements of yield strength have some uncertainty associated with the assumption of a circular GB area and the competing effects of sintering and creep at low strain rates. Thus, the agreement cited, $\sigma_{\rm V} \approx \sigma_{\rm s.c.}$, should be taken as magnitude agreement rather than exact agreement. The quoted stresses for sintering are also somewhat approximate because a finite value is being ascribed to a probability distribution and because particle rotation observed during the experiment causes the crystallographic character of the boundary to evolve slowly in time.

The surface energy of the ZrO_2 samples used in the prior work was measured explicitly using the zero-creep method, $\gamma_{\text{S}} \approx$ 1.3 J m^{-2} , under the same experimental conditions as the in situ sintering experiments. This suggests that $\frac{\zeta}{\eta} \approx 2 - 5$. η in Eq. (7) relates to the shape of the sintering stress-densification strain response [46]. The total energy available to do work, w_T , at a given sintering stress is $\delta w_T = \Omega d\sigma_s$, where Ω is the atomic or molecular volume. A variety of processes can dissipate energy during densification, such as redistribution of solute away from local thermodynamic equilibrium because of a flux, the nucleation of the strain mediating line defect, and the creation and annihilation of point defects at different stresses. An analysis of creep in cubic ZrO₂ suggested the latter process likely dissipates the most energy when solute redistribution is not active and follows the form $\delta w_s = v_f d\sigma_s$, where v_f is the point defect formation volume [35]. The ratio of work available for sintering versus work done during densification provides a basis for approximating $\eta \approx \frac{v_f}{\Omega}$. ζ is associated with the fraction of surface energy dissipated that contributes to driving densification. The term will generally capture topological and microstructural effects. For example, one major source of energy loss from this term is hypothesized to be the shrinkage and disappearance of grains that only contact a single neighbor or de-sinter due to their local topology. It is also envisioned that pore size distribution in the later stages of sintering could also influence ζ . For example, a single large pore surrounded by a dense fine grain structure may not utilize interfacial energy dissipation as efficiently as the same pore volume distributed more uniformly amongst the grains; see Supplementary Figure S4. Such effects will be the subject of future investigation, but for simplicity $\zeta\approx 1$ is assumed here. In ZrO₂ studied previously, it was found that on average $\frac{v_f}{\Omega}\approx 0.5$. If $\frac{\zeta}{\eta}\approx 2-5$ and $\eta\approx 0.5$ for bicrystal sintering experiments, then it is reasonable to expect $\zeta\approx 1$; note that it cannot exceed unity.

Fig. 3a reproduces recently published two-particle molecular dynamics simulation results from initially spherical Ni sintered at 1000 K, and Fig. 3b replots the data in terms of ε versus ($^A\!/_V$). The same ε versus ($^A\!/_V$) response, first noted by DeHoff [32] for polycrystalline sintering, is observed in both 2-particle sintering experiments and atomistic simulations. In each case, the response is also approximately linear. Assuming $\gamma_S \approx 1~J~m^{-2}$, $\sigma_{s,c} \approx 1 \times 10^8~Pa - 2 \times 10^8~Pa$ for these particles, for $\eta \approx 1$ to $\eta \approx 0.5$. The curvatures of the neck are plotted as a function of time in Fig. 3c. Also assuming $\gamma_S \approx 1~J~m^{-2}$, the sintering stress calculated from the

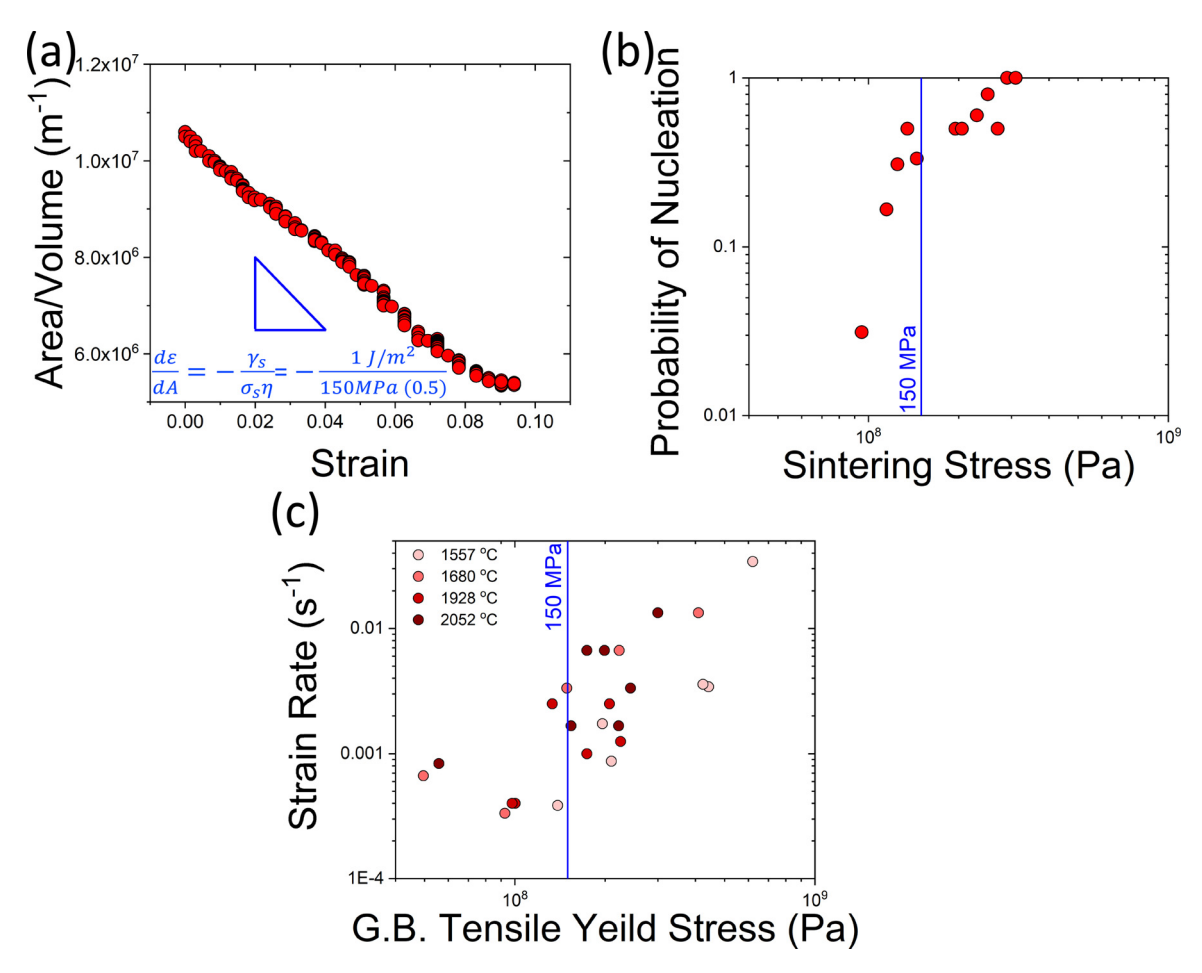


Fig. 2. (a) plot of the area to volume ratio for a single ZrO₂ particle sintering on a substrate along with the slope predicted from the model in Eq. (7) assuming $\sigma_{s,c} = 150 \text{ MPa}$. (b) Plots the probability of 'nucleating' a densification strain event as a function of sintering stress, which was used to approximate a value $\sigma_{s,c} = 150 \text{ MPa}$ for (a). (c) the relationship between strain rate and grain boundary tensile yield strength measured at several temperatures.

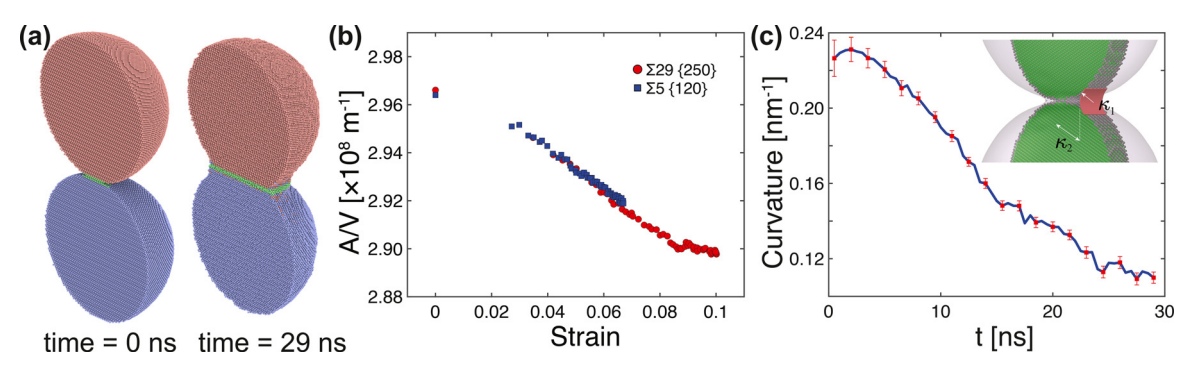


Fig. 3. (a) Cross-sectional view of a 2-particle sintering configuration at 0 ns and 29 ns during MD simulations performed at 1000 K using a Ni potential, (b) a plot of the interfacial area density versus densification strain, and (c) plot of the mean curvature at the neck versus time.

curvature is also $\sigma_{s,c}\approx 1\times 10^8 Pa-3\times 10^8 Pa$. Uncertainty exists when calculating curvatures from MD data and the value of η . The MD simulations, nevertheless, suggest that to within a factor of 2, $\frac{\zeta}{\eta}\approx 1-2$. This implies that most interfacial energy dissipated during sintering contributes directly to doing thermodynamic work on the densification process.

The surface area density varies inversely proportional to the grain radius,

$$\begin{pmatrix} A_{/V} \end{pmatrix} = \frac{B}{r} \tag{8}$$

where *B* is a geometric coefficient that should vary with grain shape, density, and microstructural topology. For the case of coars-

ening via surface diffusion, the time, t, evolution follows,

$$r^{4} - r_{o}^{4} = C \frac{D_{s} \gamma_{s} \Omega^{2} \nu}{kT} (t - t_{o}), \tag{9}$$

where C is a geometric constant, D_s is the surface diffusivity, Ω is the atomic or molecular volume, ν is the concentration of surface defects mediating diffusion, and kT is the thermal energy. Other coarsening processes such as vapor phase transport or grain boundary migration can dominate under various microstructural and processing conditions. A power law with grain size exponent on the order of 3 to 4 is, however, anticipated through the early and intermediate stages of sintering. For our discussion below, B=3 was assumed based on a spherical grain approximation,

which is a minimum value and could slightly underestimate the area density of polyhedral grains. C = 10 was assumed for evaluating coarsening rates in context of the model described by Nichols and Mullins [46].

Equations (7) through (9) provide the basis for an initial stage sintering model that accounts for the observations that densification follows interface nucleation rate limited kinetics and is thermodynamically coupled to surface energy dissipation associated with coarsening. Of the constants in this model, $\sigma_{s,c}$ likely exhibits the largest variability and most greatly influences sinterability, its magnitude and temperature dependence, however, are not well understood. Supplementary Figure S5 shows example numerical predictions from the model for sintering of materials with two different initial grain sizes and densities as a function of temperature assuming $\sigma_{s,c}$ decreases with increasing temperature. These data predict that increased heating rate, decreased initial grain size, and increased initial density all promote densification in agreement with experimental trends within the literature. This suggests the model could be appropriately applied to sintering experiments. If, alternatively, $\sigma_{s,c}$ is assumed to be constant, as shown in Figure S6, then there is no heating rate dependence to the sintering trajectory. A heating rate dependence of the sintering trajectory, where high heating rates favor enhanced densification relative to coarsening, is well known experimentally [13,15,26]. An inherent feature of the model is its ability to simply predict sintering trajectories for different conditions of initial particle size, density, and sintering schedule. What is required here is a better understanding of how $\sigma_{s,c}$ varies as a function of temperature in real materials and how that, in turn, influences sintering. $\sigma_{s,c}$ should generally vary with temperature following Boltzmann statistics,

$$\sigma_{s,c} = \frac{-kT ln \frac{\dot{\varepsilon}}{\dot{\varepsilon}_o} - H^* + S^*T}{v^*}$$
 (10)

where H^* and S^* are the activation enthalpy and activation entropy, respectively. The following section emphasizes measuring $\sigma_{s,c}(T)$ at an interface of a single misorientation to avoid uncertainties associated with measurements of random interfaces or distributions of interfaces.

4. Experimental results

The high aspect ratio pearl necklace structures characterized in this study should tend to densify forming shorter and wider grains [45]. Coarsening of the entire structure over time should drive mass away from the overall pearl necklace structure towards low curvature surfaces on the substrate. The surface diffusivity of Al₂O₃ exceeds that of GdAlO₃ by more than an order of magnitude [47], and at longer timescales Al₂O₃ may also preferentially evaporate. The degree of evaporation-condensation versus surface diffusion, however, does not affect the thermodynamic analysis presented herein. Fig. 4 shows the evolution of a specimen tested at 1688 °C. The Al₂O₃ portions of the sample clearly evolve faster than the GdAlO₃ consistent with the expectations of faster Al₂O₃ transport kinetics. No apparent densification strain is observed during the initial portion of the experiment, despite the sintering stress being on the order of 10^7 Pa, assuming $\gamma_s \sim 1$ J m^{-2} , which would drive a densification rate of $\sim 5000 \ nm \ s^{-1}$ at random boundaries [47]. The densification strain observed, however, is effectively zero within experimental measurement error. The sintering potential only varies weakly with time, but the sintering stress tends to increase as the interfacial area reduces. When the sintering stress increases above a critical value the adjoining Al₂O₃ particle undergoes rapid rigid body rotation and displacement that is associated with densification. The rate of rigid body motion is fast relative to the temporal resolution of the experiment, which makes calculating a diffusivity challenging. This rapid rigid body motion, nevertheless, implies that the diffusion coefficient at the interface is sufficiently high that transport should have been observable at earlier points in time had appropriate unsaturable vacancy sinks existed. Interfaces in these same samples were previously characterized via high resolution TEM. The orientation relationship can be described by $[2\bar{2}01]Al_2O_3 \parallel [1\bar{1}0]GdAlO_3$ and $(01\bar{1}2)Al_2O_3 \parallel (001)GdAlO_3$. Example high resolution TEM images are shown in supplementary Figure S7. The lattice mismatch of \approx 5% is accommodated by misfit dislocations every 18-19 atomic planes. These misfit dislocations, however, cannot mediate axial strain via climb because such climb would occur out of the interfacial plane, see schematic in Supplementary Figure S8. The kinetic observations made herein, i.e. that densification is much slower than predicted by interfacial diffusivity and occurs discontinuously above a critical driving force, are generally consistent with a hypothesis that the interfacial transport is interface nucleation rate limited. The trend is similar to recent molecular dynamics simulations of diffusion and sintering performed using Ni particles [48].

Fig. 5 shows a series eutectic interfaces undergoing similar microstructural evolution, wherein the Al₂O₃ preferentially shrinks, the interfacial area reduces, and rapid rigid body motion occurs after a relatively long incubation period. A decrease in temperature is clearly associated a smaller interfacial area at which the particle undergoes rigid body motion. This corresponds to a higher sintering stress as shown in Fig. 6, which plots the critical sintering stress necessary to induce strain versus temperature. A linear fit to the data in Fig. 6 produces, $\sigma_{s,c}(T) = -2.03 \times 10^6 T + 4.03 \times 10^9$ where *T* is in K. A linear fit is likely not the most appropriate form but is used here for simplicity. The spread in the data at each temperature is anticipated to reflect the statistical nature of the nucleation process but could also represent some uncertainty introduced from the assumption of 3-dimensional axial symmetry, i.e. the GB area. Thirteen independent measures made at 1845 K can be used to approximate an activation volume at this temperature, $v^*=12.5 \vec{b}^3 \pm 3 \vec{b}^3$ where \vec{b} is the Burgers vector. The data also suggest that at temperatures close to the onset of sintering in Al2O3 the critical stress is close to a GPa. This is qualitatively consistent with observations that constrained sintering at low temperatures, close to the onset of sintering, can evolve GPa level residual stresses [31].

The activation enthalpy may be calculated as [37]

$$H^* = -T \left(\frac{\partial \sigma^*}{\partial T} \right)_{\dot{\varepsilon}} \nu^*. \tag{11}$$

The fit of the experimental data in Fig. 6 is used to approximate $(\frac{\partial \sigma^*}{\partial T})_{\dot{\epsilon}} = -2.0 \times 10^6 \pm 0.1 \ Pa \ K^{-1}$, which is cited as an approximation because the densification strain rate at nucleation cannot be fixed. The data form the basis for approximating an activation enthalpy, $H^* = 4.8 \text{ eV}$, which should be of the correct order of magnitude. The large activation energy supports the hypothesis that the associated nucleation processes should be rate limiting for densification in this system. The activation energy for yield of ZrO₂ general bicrystal grain boundaries was $H^* = 1.9 \text{ eV}$ [35,36]. The eutectic interface is anticipated to be relatively low energy, for example the average surface dihedral angle is 128 ° while the average surface dihedral angle at random Al₂O₃-GdAlO₃ interfaces is 113 °. As a result, this activation energy may be large relative to that associated with higher energy interfaces, such as random grain boundaries in ZrO₂. Recent efforts have been made to calculate activation energies for the nucleation of distributions of grain boundary disconnections in simple metals [49], but the reported results are difficult to compare with the current experimental results. The magnitude, nevertheless, indicates that the barrier is quite large and highlights the potential need for a model that considers this nucleation step as rate limiting.

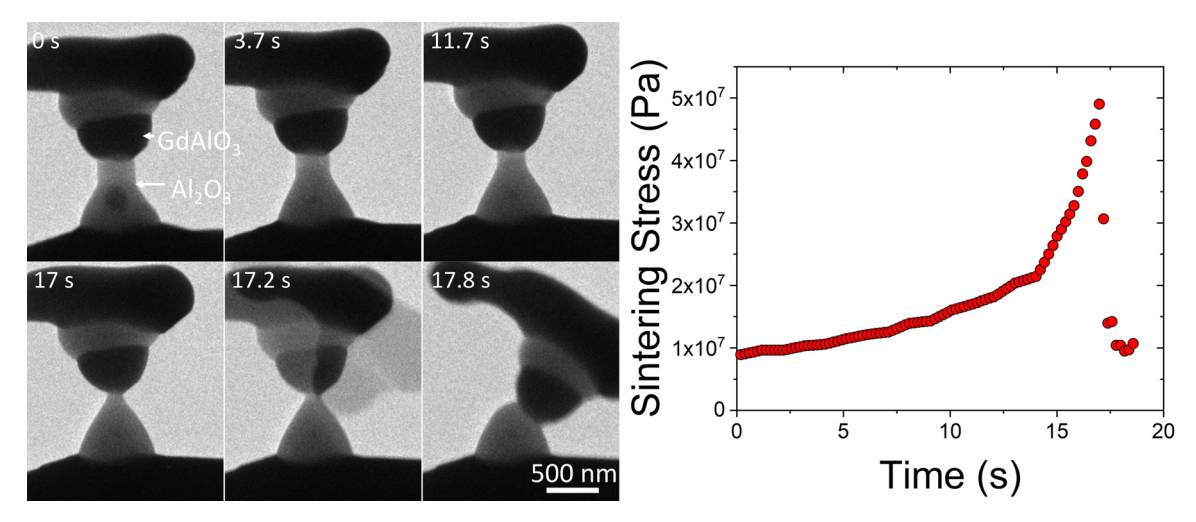


Fig. 4. The microstructural evolution of the eutectic structure under annealing at 1688 °C. The neck reduces in area as Ostwald ripening reduces the volume of the Al_2O_3 grain (brighter phase). During this process no rigid body motion that would be associated with transport at the Al_2O_3 -GdAlO₃ interface is observed. The reduction in solid-solid interfacial area increases the sintering stress to the point at which rigid body motion is activated, at which point rapid transport occurs. This stress is taken as the critical stress necessary to induce interfacial transport, $\sigma_{s,c}$.

The sintering potential, $\Sigma_s = \sigma_s A_g$, can be used to calculate the change in Gibbs free energy, $\mathrm{d}G = \Sigma_s dl$, where dl is the change in length associated with rigid body motion. Since dl occurs over a short interval relative to the total process, the changes in free energy associated with the entire densification event, $\Delta G_T = \int \Sigma_s dl$, and the change just before and after rigid body motion at the critical stress, $\Delta G_{s,c} = \int \Sigma_{s,c} dl$, provide a measure of the efficiency of the work of sintering $\frac{\delta w_s}{\delta w_T} \approx \frac{\Delta G_{s,c}}{\Delta G_T} = \frac{\Sigma_{s,c}}{\Sigma_s} = \eta$; see supplementary Figure S9 for additional details. Just prior to the onset of rigid body motion some amount of stored energy is present at the sintering neck that relaxes during densification, and η is envisioned to describe how much of that stored energy must go into performing thermodynamic work to drive densification. The calculated value of $\eta \approx 0.8 - 0.9$ is insensitive to temperature. This implies that most of the excess free energy in the activated state must go into driving densification.

The motivation for developing the model derived largely from two-particle model experiments. Before extending it to analysis of a bulk system it would be prudent to preliminarily test the model in context of multiparticle sintering. In this case, Al₂O₃-GdAlO₃ nanoparticles were sintered in situ at 1491 °C, see Fig. 7. The approximately linear relationship between ${}^{A}\!\!/_{\!\! V}$ and ε can be observed and application of the model suggests $\sigma_{s.c} \approx 2 \times 10^8 \ Pa$. This same cluster was sintered at lower temperatures for similar amounts of time, and although some coarsening was observed little densification was measurable. This is consistent with an expectation that $\sigma_{s,c}$ should be higher at lower temperatures. The eutectic boundary should exhibit a value of $\sigma_{s,c} \approx 4 \times 10^8 \ Pa$ at this temperature. Random high energy boundaries are anticipated to produce a lower value of $\sigma_{s,c}$ than the low energy eutectic interface, thus the agreement is reasonable. In prior experiments, the surface diffusivities of Al₂O₃ and GdAlO₃ were measured to be $D_s = 3.5 \times 10^{-13} \ m^2 \ s^{-1}$ and $D_s = 1.4 \times 10^{-14} \ m^2 \ s^{-1}$ at 1491 °C, respectively [47]. Applying our model to the in situ sintering of an Al₂O₃-GdAlO₃ nanoparticle cluster shown in Fig. 7 produces an average value $D_s = 1.3 \times 10^{-13} \ m^2 \ s^{-1}$. The model fit appears to agree well with the average values measured from capillary smoothing experiments. Note that utilizing the surface diffusivity within the model likely only works for low densities, such as shown in Fig. 7, when the effects of grain boundary migration on coarsening are limited.

Since the interface nucleation rate limited model appears to fit multiparticle sintering data well, as highlighted by the data in Fig. 7, it is reasonable to ask whether the model can predict bulk sintering behavior. Since no bulk sintering kinetics data is available to Al₂O₃-GdAlO₃, prior data for Sc₂O₃-doped ZrO₂ is used as a general proxy for ZrO₂ materials. The model is parameterized assuming $\zeta=1$, $\eta=0.5$, and $\gamma_S=1$ J m^{-2} and based on experimentally determined $\sigma_{s,c}(T)$ from bicystal sintering and creep experiments. Fig. 8a plots experimental sintering trajectories and trajectories calculated using our model based on the initial values of density, grain size and temperature from the experiments. The density, ρ , is given by the initial value, ρ_o , plus the densification strain;

$$\rho = \rho_0 + \varepsilon \tag{12}$$

Assuming $\zeta \neq f(A_{V})$, integrating Eq. (7) and combining it with (12), predicts a sintering trajectory in the form of;

$$\rho = \rho_0 + \frac{\gamma_s \left(\frac{A}{V} - \frac{A_0}{V_0} \right) \zeta}{\sigma_{s,c} \eta} \tag{13}$$

The experimental data in Fig. 8a represent a range of different chemistries and starting materials, which introduces inherent scatter for sintering of oxides, see discussion of Al₂O₃ versus metal sintering below. The model, nevertheless, captures the broad trends in sintering trajectory quite well without invoking any fitting parameters. Such a prediction, without invoking fitting parameters, would be challenging based on traditional sintering models. It is not obvious that the model should extend to the final stages of sintering but is hypothesized here to be effective in the range where coarsening is pore-drag limited. It is anticipated that the coarsening kinetics will not follow Eq. (9) beyond the initial stages of sinter, but the relation in Eq. (7) is anticipated to remain valid through initial and intermediate stages of sintering. Verifying the conditions under which the model assumptions break down will be the subject of future work.

The model should also be checked to ensure that it can reasonably fit isothermal temporal evolution for both grain growth and densification. In this case, $\sigma_{s,c}$ and D_s are taken as fitting parameters assuming $\zeta=1$, $\eta=0.5$, and $\gamma_S=1$ J m^{-2} . Data were fit using an iterative approach to converge on a solution for both $\sigma_{s,c}$ and σ_s . This approach utilized an initial guess for both values and varied them within a Matlab script until the error between the cal-

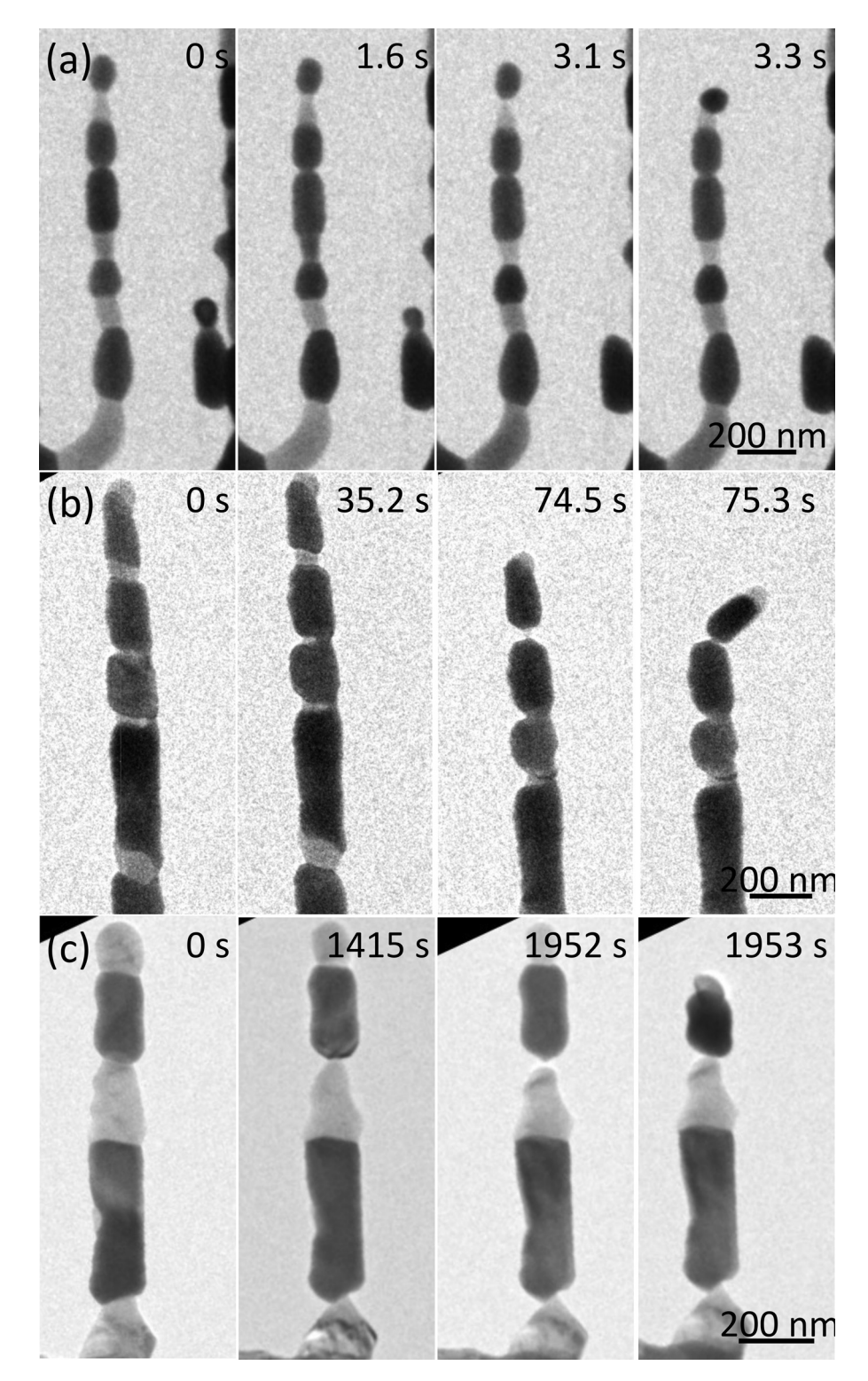


Fig. 5. The microstructural evolution of the eutectic structure at (a) 1637 °C, (b) 1572 °C, and (c) 1262 °C. Note that as the temperature decreases the width of the neck at which rigid body motion is activated also decreases indicating that the critical stress, $\sigma_{s,c}$, increases.

culated curve and the experimental data was minimized. Fig. 8b provides example isothermal sintering data fits using data from He and Ma [50]. This data was selected because they considered two initial grain sizes of different magnitude and fit their data to both a diffusion limited model and an interface rate limited model of a different form, i.e. interface point defect emission and absorption

limited. Within experimental error, the current model may also be fit to this data. Independently fitting $\sigma_{s,c}$ and D_s at each of the six temperatures produces R-squared values $R^2 > 0.95$ in each case. The good fit indicates that our model cannot be distinguished from a Coble type model [19] or an Ashby type model [21] on the basis of isothermal fitting.

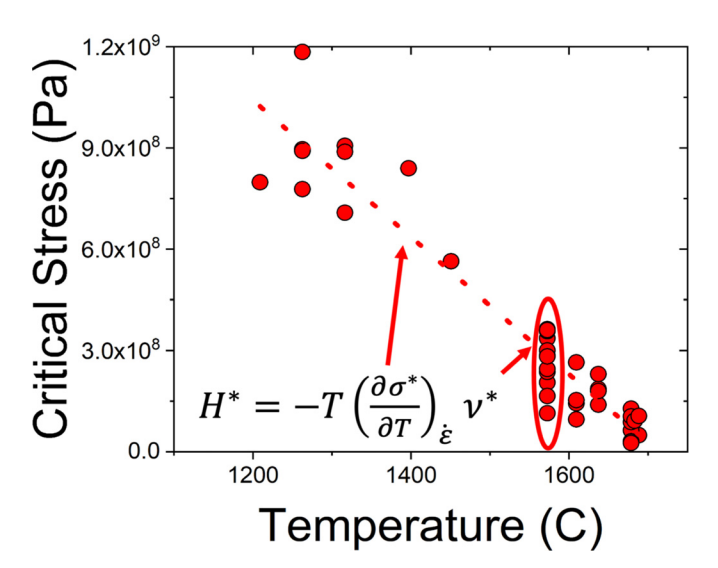


Fig. 6. The temperature dependence of $\sigma_{S,c}$ based on a series of independent measurements. The temperature dependence of the critical stress and the activation volume provide a basis for approximating the activation enthalpy.

Given the reasonable fit provided by the model, one may anticipate that an approximate value of $\sigma_{s,c}$ could be extracted from literature data assuming $\zeta=1$, $\eta=0.5$, and $\gamma_S=1$ J m^{-2} . Performing such calculations for Al₂O₃ produces considerable scatter when plotted as $\sigma_{s,c}$ versus homologous temperature as shown in Fig. 9a. Al₂O₃ kinetics tend to be highly sensitive to impurities and dopants so the system may not be an ideal test. Fig. 9b plots $\sigma_{s,c}$ versus homologous temperature data for simple metals and alloys fit under the same assumptions, $\zeta=1$, $\eta=0.5$, and $\gamma_S=1$ J m^{-2} . $\sigma_{s,c}$ decreases with temperature, as anticipated, and the data for

all fall within a range of a factor of 2 at any given homologous temperature. Comparison of Figs. 9a and 9b highlight major differences in the sintering response of metals and oxides. Since lower values of $\sigma_{s,c}$ represent higher sinterability, the data suggest that Al_2O_3 is less sinterable than simple metals. The values of $\sigma_{S,C}$ in both data sets are of comparable magnitude to bulk yield and flow stresses in Al₂O₃ and metals at equivalent homologous temperatures [51]. This qualitatively aligns with the inherent assumption in the model that the process is rate limited by the nucleation of high energy grain boundary dislocations, where 'high energy' here implies some large fraction of the bulk dislocation energy. Employing our model to analyze polycrystalline sintering data in detail as a function of temperature and chemistry and extending it to predicting sintering response is beyond the scope of the current manuscript and will be the subject of future work. These data were introduced here, nevertheless, to provide some insights into the next logical steps in employing our model to understand the literature or make engineering predictions.

One additional consideration in the temperature dependence of sintering trajectory is the temperature dependence of the propensity for de-sintering. Fig. 7 shows an example of de-sintering occurring during in situ sintering of an Al₂O₃-GdAlO₃ particle ensemble resting on a dense polycrystalline Al₂O₃-GdAlO₃ substrate. Several examples of de-sintering are observed in this data. A complete discussion of the phenomena is outside of the scope of this paper. Sudre and Lange [30] provided an approximate solution for the de-sintering condition in terms of the ratio of grain length to grain diameter $\frac{L}{D} > 1.36$ for a dihedral angle of 120 °. De-sintering occurs in the Al₂O₃-GdAlO₃ cluster when $\frac{L}{D}=1.34\pm0.12$ in good agreement with this model, see Fig. 7. The particles that de-sinter appear to approach this condition because Ostwald ripening drives a reduction in particle volume while the rate of densification does not proportionally reduce the length of the bridging particle distance. This situation was also hypothesized by Lange [52]. Since

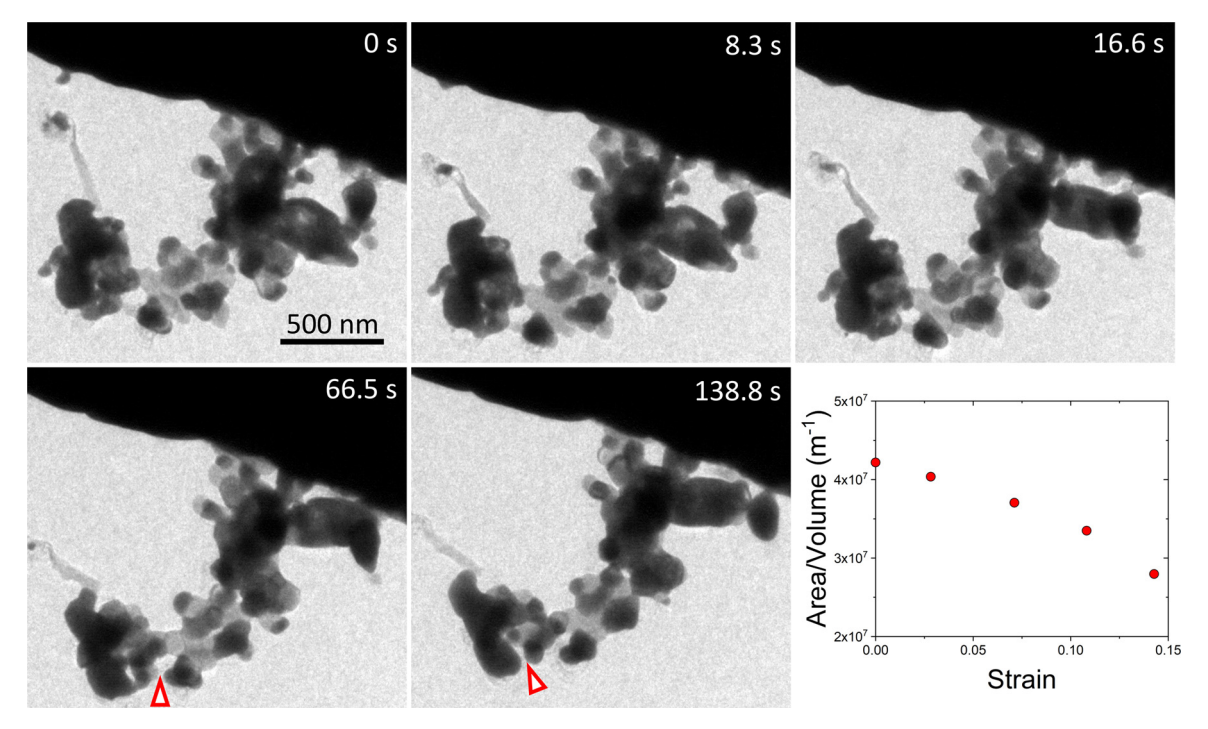


Fig. 7. In situ TEM image sequence showing the sintering of a cluster of Al_2O_3 (bright phase) – GdAlO₃ (dark phase) particles resting on a dense substate of polycrystalline Al_2O_3 –GdAlO₃ at 1491 °C. The red triangles in the figure highlight several places where de-sintering was observed during sintering. The de-sintering is hypothesized to result from shrinkage of small particles whose volume reduces fast relative to the rate of shrinkage that causes it to approach the critical condition for de-sintering. The figure plots the area to volume ratio as a function of densification strain. The densification strain was approximated from the change in projected area, while the area/volume was approximated manually by tracing the particles and directly measuring the perimeter/area, the mean value is plotted in the figure. The linear fit to the data is -9.7×10^8 m $^{-1}$.

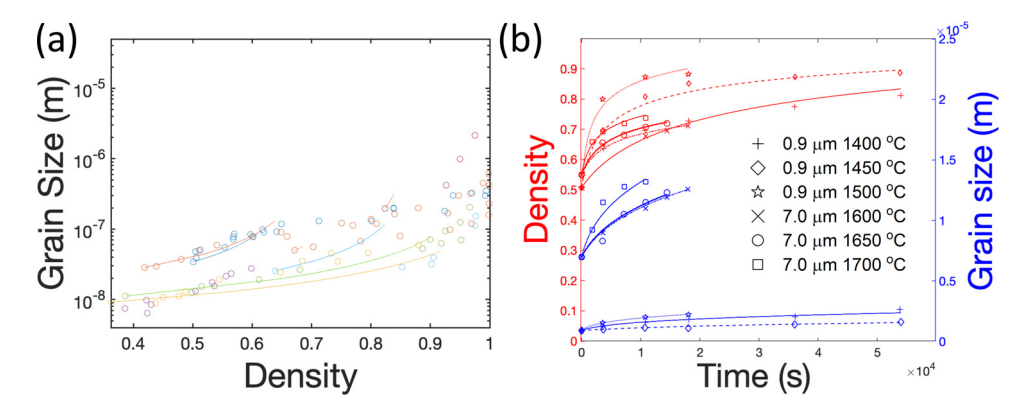


Fig. 8. a) data from references [27,66-69] for sintering of ZrO₂ materials fit to a model parameterized based on prior in situ bicrystal sintering and creep in Sc₂O₃-doped ZrO₂ [35,36]. The sintering trajectories, i.e. density versus grain size, are predicts from the model without invoking fitting parameters. The open circles represent the experimental values while the lines represent the predicted trajectories. The general trends are captured well by the model, although each specific experiment is anticipated to have some variability due to differences in chemistry. b) Example fit of the model developed in this work to isothermal Al₂O₃ sintering data for both grain size and density as a function of time reported in reference [50]. Here no assumptions are made about the physical constants in the model and is instead a pure fit to the functional form of the model. The model can capture the general response of both the density and grain size evolution in time.

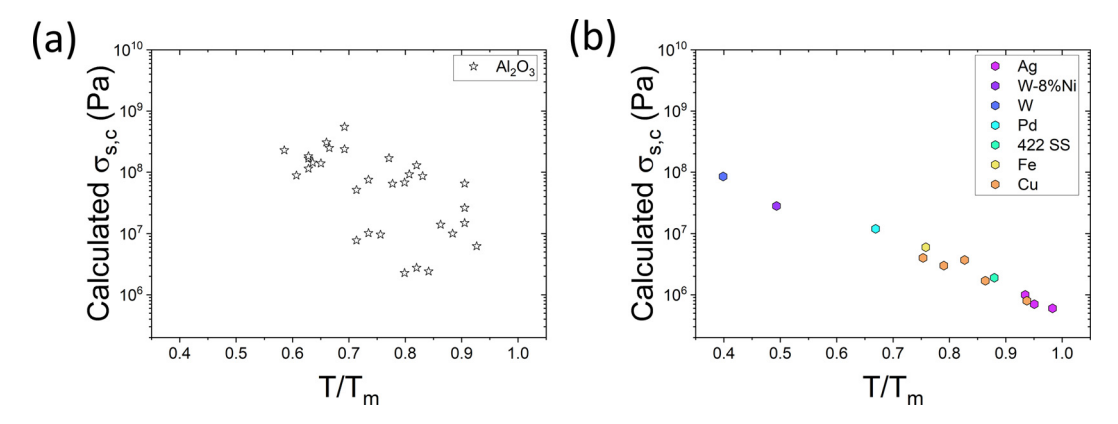


Fig. 9. Calculated values for $\sigma_{s,c}$ versus homologous temperature obtained by fitting experimentally reported grain size-density trajectory data from the literature assuming $\eta = 0.5$ and $\gamma_S = 1$ J m^{-2} . The magnitude of $\sigma_{s,c}$ is hypothesized to provide a measure of the sinterability of a system, since it describes the grain-size density trajectory. (a) plots data for undoped Al_2O_3 which exhibits a large amount of scatter, (b) plots data for metallic systems. The data for metallic systems is quite consistent and provides an indication that the model could be physically reasonable, while the data for ceramics is much more scattered, possibly due to the sensitivity of these systems to impurities. Data from references [50,70-88].

our model predicts that the ratio of the rates of coarsening to densification are temperature dependent, then it implies that the amount of de-sintering should also be temperature dependent. This effect would show up in the value of ζ in our model, which would have a temperature dependence for the reasons discussed above. This is likely important during the initial stages of sintering when de-sintering is more likely due to topological considerations. Based on our in situ TEM observations of sintering, such as in Fig. 7, it is hypothesized that de-sintering likely does not diminish ζ significantly. The process can, however, lead to the evolution of larger than average pores that could impact the later stages of sintering, as observed in Fig. 7 and continuum scale simulations of sintering [53].

5. Discussion

The final point about de-sintering returns us to the initial discussion in the background section. It was argued that GB dislocation nucleation had been discounted as a rate limiting mechanism in sintering, and creep, because the processes occur at average stresses too low to nucleate such dislocations. A key question of interest then is how capillary processes overcome large activation barriers during microstructural evolution. During de-sintering of a GB, it must approach the work of adhesion and the correspondingly high theoretical GB fracture stress. Simplistically, this

stress largely derives from the tensile force imposed by the surface energy, which is approximately constant, the angle at which this force is applied, and the area over which the force is applied. In this context, the basis for our model is reasonably intuitive. If the driving force for some capillary driven process, such as sintering, exists but the barrier for nucleating a strain mediating GB dislocation is large relative to the instantaneous driving force, then the area of the GB may decrease, or the dihedral angles at the triple junctions may vary, in a manner that increases the local stresses at the boundary and/or 3-grain and 4-grain junctions until the barrier can be overcome. The rate at which this occurs will be proportional to the rate of change in the total interfacial area and must preserve free energy. These conditions naturally lead to equations (7) through (9). Few direct analogs have been considered within the literature, but several related phenomena have been discussed. Supplementary Figure S10 schematically depicts several situations discussed below. De-pinning of grain boundaries from pores or second phase particles can occur during grain growth. The barrier for de-pinning is often large relative to the driving force when the boundary first bisects the particle. GB migration can, however, push the dihedral angles at the particle-grain boundary triple line away from their local equilibrium configuration and towards a direction where the GB applies a larger de-pinning force on the particle [54]. If the particle is subject to shrinkage this provides another pathway for increasing the local stress on the parti-

cle applied via capillary action. As an alternative example, molecular dynamics simulations demonstrate that GBs respond in a similar manner when the nucleation of a vacancy is geometrically necessary during GB migration. In this case, the GB geometry varies in a manner that applies a larger local stress on the region where the vacancy nucleates [55]. Similar observations have been made with respect to occlusion of solute clusters during GB migration subject to solute drag [56]. Molecular dynamics simulations also indicate that large local stresses evolve at triple junctions during GB migration, which facilitate geometrically necessary disconnection reactions there [57].

Detailed discussion of how this model fits into other aspects of sintering science are outside of the scope of this manuscript. It is envisioned, however, that the model can account for the linear effects of applied pressure during hot pressing through a linear reduction in $\sigma_{s,c}$ [58]. The magnitude of $\frac{d\varepsilon}{d(A_{V)}}$ should vary in-

versely proportional to the applied stress, which is a testable hypothesis. Stress concentration at particle contacts would, nevertheless, be necessary to increase local driving forces to magnitudes comparable to $\sigma_{s,c}$ [59]. The same general model might also apply well to cold sintering [16], typically performed at applied stresses of $\sigma > 10^8$ Pa that could bring local stresses at GB contacts to values comparable to $\sigma_{s,c}$ at low temperatures. Cold sintering exhibits coarsening and could follow the general framework of the model, wherein coarsening drives local stress concentrations that can induce GB mediated plasticity that drives densification. Our model can potentially account for the effects of shear stresses in accelerating densification [60,61], through their role in modifying H^* and by extension $\sigma_{s,c}$. The model might explain why an initial high temperature step in two-step sintering can modify the pore size distribution, which enables efficient densification in the second step [27]. This could occur by reducing the amount of desintering occurring in the initial stage by accelerating the rate of densification relative to coarsening. The model might explain the evolution of anomalously large residual stresses[31] in poorly densifying systems, and the ability of high heating rate high temperature sintering to reduce residual stress during constrained sintering [13,62], through the influence of $\sigma_{s,c}(T)$. Note that below $\sigma_{s,c}$ residual stresses should not be relaxed efficiently by densification or Coble creep. The magnitude of $\sigma_{s,c}$ in different classes of materials, e.g. metals, oxides, nitride, carbides, etc. may provide insights into their relative sinterabilities. The nature of interfacial defect nucleation in interfaces of different GB structures could provide deeper insights into the role of disordered interfacial phases in promoting so-called activated sintering [63,64]. At the current moment, considerable ongoing work is required to test some of the hypotheses invoked in this paragraph. The current model, however, does not appear, at first pass, to be qualitatively inconsistent with any broadly observed trends in the sintering literature. It could, in fact, provide a new framework for understanding poorly understood sintering phenomena. In fact, when the critical sintering stress, $\sigma_{s,c}$, greatly exceeds the average sintering stress in the system, then a dissipative model of some form must be invoked to explain densification. Dissipative models for disconnection mediated grain growth have recently been reported to describe the process well [65]. For systems with low critical sintering stresses and/or high driving forces, e.g. nanograined particles or large applied stresses, then sintering kinetics will approach the diffusion limited solution, e.g. Coble's model. The model may also form a basis for new mechanism informed design of sintering schedules, possibly driven by computationally predicted materials properties.

Finally, Ashby's [21] original explanation for interface rate limited kinetics during creep cited the stress dependence of point defect emission from and absorption to GB dislocations. In that work, he further speculated that analogous ideas should extend to densi-

fication during sintering. Our work here implies that densification may be rate limited by the nucleation of point defect sources and sinks. Logically, it may be reasonable to expect this mechanism to extend to interface nucleation rate limited creep problems. Ashby's model is often ascribed to observations of power law stress exponents $n \geq 2$ during interfacial creep and the existence of a threshold stresses for inducing creep.

6. Conclusions

Recent in situ TEM based observations of interface nucleation rate limited sintering kinetics were used as the basis for formulating a simple analytical model to describe the relationship between coarsening and densification during sintering. The model extends general relations between these parameters first noted by DeHoff and coworkers [32] by relating their scaling constant to materials properties. Model experiments were used to demonstrate interface nucleation rate limited kinetics at Al₂O₃-GdAlO₃ interfaces, as well as derive the temperature dependence, and activation free energy for the process. The model was shown to fit in situ sintering data for particle clusters well. Critical stresses associated with overcoming the nucleation barrier for the interface nucleation rate limited kinetic process were used to parameterize the sintering model, which predicted realistic sintering trajectories without invoking fitting parameters. The model was also demonstrated to fit isothermal sintering data from the literature well.

Declaration of Competing Interest

The authors declare that they have no known competing financial interests or personal relationships that could have appeared to influence the work reported in this paper.

Acknowledgments

Support from National Science Foundation under Grant DMR 1922867 is acknowledged by K.C and S.J.D. FA and OH acknowledges support from the National Science Foundation under Grant No. OIA 2033327. C.M.B. and K.H. were supported by the DOE-BES Materials Science and Engineering Division under FWP 15013170. This work was performed, in part, at the Center for Integrated Nanotechnologies, an Office of Science User Facility operated for the U.S. Department of Energy (DOE) Office of Science. Sandia National Laboratories is a multimission laboratory managed and operated by National Technology and Engineering Solutions of Sandia, LLC, a wholly owned subsidiary of Honeywell International, Inc., for the U.S. DOE's National Nuclear Security Administration under contract DE-NA-0003525. The views expressed in the article do not necessarily represent the views of the U.S. DOE or the United States Government, Y.H.M acknowledges support from the Fundamental Research Funds for the Central Universities under No. 3072022TS2702 and Jh.O. acknowledge Natural Science Foundation of China for the supports in this work under Grant Nos. 51972085, 51572061 and 51621091.

Supplementary materials

Supplementary material associated with this article can be found, in the online version, at doi:10.1016/j.actamat.2022.118448.

References

- [1] J. Banhart, Manufacture, characterization and application of cellular metals and metal foams, Prog. Mater. Sci. 46 (6) (2001) 559–632.
- 2] D.R. Clarke, Varistor ceramics, J Am Ceram Soc 82 (3) (1999) 485–502.
- [3] W.G. Fahrenholtz, G.E. Hilmas, I.G. Talmy, J.A. Zaykoski, Refractory diborides of zirconium and hafnium, J Am Ceram Soc 90 (5) (2007) 1347–1364.

[4] D.D. Gu, W. Meiners, K. Wissenbach, R. Poprawe, Laser additive manufacturing of metallic components: materials, processes and mechanisms, Int. Mater. Rev. 57 (3) (2012) 133–164.

- [5] T.W. Hansen, A.T. De La Riva, S.R. Challa, A.K. Datye, Sintering of Catalytic Nanoparticles: particle Migration or Ostwald Ripening? Acc Chem Res 46 (8) (2013) 1720–1730.
- [6] H. Inaba, H. Tagawa, Ceria-based solid electrolytes, Solid State Ionics 83 (1,2) (1996) 1–16.
- [7] C. Piconi, G. Maccauro, Zirconia as a ceramic biomaterial, Biomaterials 20 (1) (1998) 1–25.
- [8] M.T. Sebastian, H. Jantunen, Low loss dielectric materials for LTCC applications: a review, Int. Mater. Rev. 53 (2) (2008) 57–90.
- [9] R.K. Bordia, S.-J.L. Kang, E.A. Olevsky, Current understanding and future research directions at the onset of the next century of sintering science and technology, J. Am. Ceram. Soc. 100 (6) (2017) 2314–2352.
- [10] K.T. Faber, T. Asefa, M. Backhaus-Ricoult, R. Brow, J.Y. Chan, S. Dillon, W.G. Fahrenholtz, M.W. Finnis, J.E. Garay, R.E. García, Y. Gogotsi, S.M. Haile, J. Halloran, J. Hu, L. Huang, S.D. Jacobsen, E. Lara-Curzio, J. LeBeau, W.E. Lee, C.G. Levi, I. Levin, J.A. Lewis, D.M. Lipkin, K. Lu, J. Luo, J.-P. Maria, L.W. Martin, S. Martin, G. Messing, A. Navrotsky, N.P. Padture, C. Randall, G.S. Rohrer, A. Rosenflanz, T.A. Schaedler, D.G. Schlom, A. Sehirlioglu, A.J. Stevenson, T. Tani, V. Tikare, S. Trolier-McKinstry, H. Wang, B. Yildiz, The role of ceramic and glass science research in meeting societal challenges: report from an NSF-sponsored workshop, J. Am. Ceram. Soc. 100 (5) (2017) 1777–1803.
- [11] J.E. Smay, J.A. Lewis, in: Solid Free-Form Fabrication of 3-D Ceramic Structures, John Wiley & Sons, Inc., 2012, pp. 459–484.
- [12] M. Cologna, B. Rashkova, R. Raj, Flash sintering of nanograin zirconia in <5s at 850°C, J Am Ceram Soc 93 (11) (2010) 3556–3559.
- [13] C. Wang, W. Ping, Q. Bai, H. Cui, R. Hensleigh, R. Wang, A.H. Brozena, Z. Xu, J. Dai, Y. Pei, C. Zheng, G. Pastel, J. Gao, X. Wang, H. Wang, J.-.C. Zhao, B. Yang, X. Zheng, J. Luo, Y. Mo, B. Dunn, L. Hu, A general method to synthesize and sinter bulk ceramics in seconds, Science 368 (6490) (2020) 521–526.
- [14] J. Hong, L. Gao, S.D.D.L. Torre, H. Miyamoto, K. Miyamoto, Spark plasma sintering and mechanical properties of ZrO2(Y2O3)-Al2O3 composites, Mater. Lett. 43 (1–2) (2000) 27–31.
- [15] W. Ji, B. Parker, S. Falco, J.Y. Zhang, Z.Y. Fu, R.I. Todd, Ultra-fast firing: effect of heating rate on sintering of 3YSZ, with and without an electric field, J. Eur. Ceram. Soc. 37 (6) (2017) 2547–2551.
- [16] J. Guo, H. Guo, A.L. Baker, M.T. Lanagan, E.R. Kupp, G.L. Messing, C.A. Randall, Cold Sintering: a Paradigm Shift for Processing and Integration of Ceramics, Angew. Chem., Int. Ed. 55 (38) (2016) 11457–11461.
- [17] J. Lu, K.-i. Ueda, H. Yagi, T. Yanagitani, Y. Akiyama, A.A. Kaminskii, Neodymium doped yttrium aluminum garnet (Y3Al5O12) nanocrystalline ceramics - a new generation of solid state laser and optical materials, J. Alloys Compd. 341 (1–2) (2002) 220–225.
- [18] M.A. Yar, S. Wahlberg, H. Bergqvist, H.G. Salem, M. Johnsson, M. Muhammed, Chemically produced nanostructured ODS-lanthanum oxide-tungsten composites sintered by spark plasma, J. Nucl. Mater. 408 (2) (2011) 129–135.
- [19] R.L. Coble, Initial sintering of alumina and hematite, J. Am. Ceram. Soc. 41 (1958) 55–62.
- [20] D.L. Johnson, New Method of Obtaining Volume, Grain-Boundary, and Surface Diffusion Coefficients from Sintering Data, J. Appl. Phys. 40 (1) (1969) 192–200.
- [21] M.F. Ashby, Interface-reaction control of Nabarro-Herring creep and sintering, Scr. Met. 3 (11) (1969) 837–842.
- [22] B. Burton, Interface reaction controlled diffusional creep: a consideration of grain boundary dislocation climb sources, Mater. Sci. Eng. 10 (1972) 9–14.
- [23] Z.Z. Du, A.C.F. Cocks, Constitutive models for the sintering of ceramic components—I. Material models, Acta Metall. Mater. 40 (8) (1992) 1969–1979.
- [24] Z. He, J. Ma, Constitutive modelling of the densification of micron-grain-sized alumina ceramics, Philos. Mag. 83 (16) (2003) 1889–1916.
- [25] D.K. Coffman, Y. Ma, C. Barr, J.-H. Ouyang, K. Hattar, S.J. Dillon, Evidence for interface-rate limited densification kinetics at Al2O3-GdAlO3 interfaces characterized by in situ ultrahigh temperature transmission electron microscopy, J. Eur. Ceram. Soc. 42 (13) (2022) 5904–5910.
- [26] M. Harmer, E.W. Roberts, R.J. Brook, Rapid sintering of pure and doped α -alumina, Trans. J. Br. Ceram. Soc. 78 (1) (1979) 22–25.
- [27] I.W. Chen, X.H. Wang. Sintering dense nanocrystalline ceramics without final-stage grain growth, Nature 404 (6774) (2000) 168–171.
- [28] C.S. Morgan, V.J. Tennery, Magnesium oxide enhancement of sintering of alumina, Mater. Sci. Res. 13 (1980) 427–436 (Sintering Processes).
- [29] L. Ogbuji, T.E. Mitchell, A.H. Heuer, Plastic deformation during the intermediate stages of sintering, Mater. Sci. Res. 13 (1980) 135–140 (Sintering Processes).
- [30] O. Sudre, F.F. Lange, The effect of inclusions on densification: III, the desintering phenomenon, J. Am. Ceram. Soc. 75 (12) (1992) 3241–3251.
- [31] J.D. Nicholas, S. Mandowara, Q. Yang, B.W. Sheldon, Effect of Sintering Aids on the Stress Evolution of Constrained Sintered Gadolinium-Doped Ceria Films, ECS Trans. 45 (1) (2012) 481.
- [32] R.T. DeHoff, R.A. Rummel, H.P. LaBuff, F.N. Rhines, The Relationship Between Surface Area and Density in the Second-Stage Sintering of Metals, in: H.H. Hausner (Ed.), Modern Developments in Powder Metallurgy, Springer, Boston, MA., 1966.
- [33] T.K. Gupta, Possible Correlation Between Density and Grain Size During Sintering, J. Am. Ceram. Soc. 55 (5) (1972) 276–277.
- [34] R.M. German, Sintering Trajectories: description on How Density, Surface Area, and Grain Size Change, JOM 68 (3) (2016) 878–884.

[35] R.L. Grosso, K.S.N. Vikrant, L. Feng, E.N.S. Muccillo, D.N.F. Muche, G.S. Jawaharram, C.M. Barr, A.M. Monterrosa, R.H.R. Castro, R.E. Garcia, K. Hattar, S.J. Dillon, Ultrahigh temperature in situ transmission electron microscopy based bicrystal coble creep in Zirconia II: interfacial thermodynamics and transport mechanisms, Acta Mater 200 (2020) 1008–1021.

- [36] K.S.N. Vikrant, R.L. Grosso, L. Feng, E.N.S. Muccillo, D.N.F. Muche, G.S. Jawaharram, C.M. Barr, A.M. Monterrosa, R.H.R. Castro, R.E. Garcia, K. Hattar, S.J. Dillon, Ultrahigh temperature in situ transmission electron microscopy based bicrystal coble creep in zirconia I: nanowire growth and interfacial diffusivity, Acta Mater 199 (2020) 530–541.
- [37] G. Taylor, Thermally-activated deformation of BCC metals and alloys, Progr. Mater. Sci. 36 (1992) 29–61.
- [38] Y.-H. Ma, Z.-.G. Wang, J.-.H. Ouyang, S.J. Dillon, A. Henniche, Y.-.H. Wang, Y.-.J. Wang, Microstructural toughening mechanisms in nanostructured Al2O3/GdAlO3 eutectic composite studied using in situ microscale fracture experiments, J. Eur. Ceram. Soc. 40 (8) (2020) 3148–3157.
- [39] Y. Waku, N. Nakagawa, T. Wakamoto, H. Ohtsubo, K. Shimizu, Y. Kohtoku, A ductile ceramic eutectic composite with high strength at 1,873K, Nature 389 (6646) (1997) 49–52.
- [40] Z. Liu, K. Iltanen, N. Chekurov, K. Grigoras, I. Tittonen, Aluminum oxide mask fabrication by focused ion beam implantation combined with wet etching, Nanotechnology 24 (17) (2013) 175304.
- [41] G.S. Jawaharram, C.M. Barr, A.M. Monterrosa, K. Hattar, R.S. Averback, S.J. Dillon, Irradiation induced creep in nanocrystalline high entropy alloys, Acta Mater. 182 (2020) 68–76.
- [42] R.L. Grosso, E.N.S. Muccillo, D.N.F. Muche, G.S. Jawaharram, C.M. Barr, A.M. Monterrosa, R.H.R. Castro, K. Hattar, S.J. Dillon, In Situ Transmission Electron Microscopy for Ultrahigh Temperature Mechanical Testing of ZrO2, Nano Lett 20 (2) (2020) 1041–1046.
- [43] G.C.C. Costa, S.V. Ushakov, R.H.R. Castro, A. Navrotsky, R. Muccillo, Calorimetric Measurement of Surface and Interface Enthalpies of Yttria-Stabilized Zirconia (YSZ), Chem. Mater. 22 (9) (2010) 2937–2945.
- [44] J.M. McHale, A. Auroux, A.J. Perrotta, A. Navrotsky, Surface Energies and Thermodynamic Phase Stability in Nanocrystalline Aluminas, Science 277 (5327) (1997) 788–791.
- [45] R.M. Cannon, W.C. Carter, Interplay of Sintering Microstructures, Driving Forces, and Mass Transport Mechanisms, J. Am. Ceram. Soc. 72 (8) (1989) 1550–1555.
- [46] F.A. Nichols, W.W. Mullins, Morphological Changes of a Surface of Revolution due to Capillarity-Induced Surface Diffusion, J. Appl. Phys. 36 (6) (1965) 1826–1835.
- [47] D.K. Coffman, Y. Ma, C.M. Barr, J.-h. Ouyang, K. Hattar, S.J. Dillon, Interphase boundary, grain boundary, and surface diffusion in Al2O3-GdAlO3 composites determined from bicrystal coble creep experiments, J. Eur. Ceram. Soc. 42 (9) (2022) 3976–3985.
- [48] O. Hussein, M. Alghalayini, S.J. Dillon, F. Abdeljawad, Unraveling the Role of Grain Boundary Anisotropy in Sintering: implications for Nanoscale Manufacturing, ACS Appl. Nano Mater. 4 (8) (2021) 8039–8049.
- [49] J. Han, S.L. Thomas, D.J. Srolovitz, Grain-boundary kinetics: a unified approach, Prog. Mater Sci. 98 (2018) 386–476.
- [50] Z. He, J. Ma, Constitutive modeling of the densification and grain growth of fine-grained alumina ceramics, Mater Sci Eng A Struct Mater 361 (1) (2003) 130–135.
- [51] A.H. Heuer, N.J. Tighe, R.M. Cannon, Plastic deformation of fine-grained alumina (Al2O3): II, basal slip and nonaccommodated grain-boundary sliding, J. Am. Ceram. Soc. 63 (1-2) (1980) 53-58.
- [52] F.F. Lange, De-sintering, A Phenonmena Concurrent with Densifictation Within Powder Compacts: a Review, in: R.M. German, G.L. Messing, R.G. Cornwall (Eds.), Sintering Technology, Marcel Dekker, New York, 1996.
- [53] F. Abdeljawad, D.S. Bolintineanu, A. Cook, H. Brown-Shaklee, C. DiAntonio, D. Kammler, A. Roach, Sintering processes in direct ink write additive manufacturing: a mesoscopic modeling approach, Acta Mater. 169 (2019) 60–75.
- [54] N. Louat, The inhibition of grain-boundary motion by a dispersion of particles, Philos. Mag. A 47 (6) (1983) 903–912.
- [55] M. Upmanyu, D.J. Srolovitz, L.S. Shvindlerman, G. Gottstein, Vacancy Generation During Grain Boundary Migration, Interface Sci. 6 (4) (1998) 289–300.
- [56] R.K. Koju, Y. Mishin, The Role of Grain Boundary Diffusion in the Solute Drag Effect, Nanomaterials 11 (9) (2021).
- [57] L. Thomas Spencer, C. Wei, J. Han, Y. Xiang, J. Srolovitz David, Disconnection description of triple-junction motion, Proc. Natl. Acad. Sci. 116 (18) (2019) 8756–8765.
- [58] M.P. Harmer, R.J. Brook, The effect of magnesia additions on the kinetics of hot pressing in alumina, J. Mater. Sci. 15 (12) (1980) 3017–3024.
- [59] E.A. Olevsky, Theory of sintering: from discrete to continuum, Mater. Sci. Eng. 23 (2) (1998) 41–100.
- [60] M.N. Rahaman, L.C. De Jonghe, R.J. Brook, Effect of Shear Stress on Sintering, J. Am. Ceram. Soc. 69 (1) (1986) 53–58.
- [61] D.N.F. Muche, J.W. Drazin, J. Mardinly, S. Dey, R.H.R. Castro, Colossal grain boundary strengthening in ultrafine nanocrystalline oxides, Mater. Lett. 186 (2017) 298–300.
- [62] S.K. Jha, R. Raj, Electric fields obviate constrained sintering, J. Am. Ceram. Soc. 97 (10) (2014) 3103–3109.
- [63] J.H. Brophy, L.A. Shepard, J. Wulff, The nickel-activated sintering of tungsten, Powder Met, in: Proc. Intern. Conf., New York, 1961, pp. 113–135. discussion 134-5.

[64] J. Luo, H. Wang, Y.-.M. Chiang, Origin of solid-state activated sintering in Bi2O3-doped ZnO, J. Am. Ceram. Soc. 82 (4) (1999) 916–920.

[65] I. Chesser, T. Yu, C. Deng, E. Holm, B. Runnels, A continuum thermodynamic

- framework for grain boundary motion, J. Mech. Phys. Solids 137 (2020) 103827.
- [66] J. Binner, K. Annapoorani, A. Paul, I. Santacruz, B. Vaidhyanathan, Dense nanostructured zirconia by two stage conventional/hybrid microwave sintering, J. Eur. Ceram. Soc. 28 (5) (2008) 973-977.
- [67] H. Li, S. Dey, R.H.R. Castro, Kinetics and thermodynamics of densification and grain growth: insights from lanthanum doped zirconia, Acta Mater. 150 (2018) 394-402
- [68] W. Li, L. Gao, Rapid sintering of nanocrystalline ZrO2(3Y) by spark plasma sintering, J. Eur. Ceram. Soc. 20 (14) (2000) 2441–2445.
- [69] M. Mazaheri, M. Valefi, Z.R. Hesabi, S.K. Sadrnezhaad, Two-step sintering of nanocrystalline 8Y2O3 stabilized ZrO2 synthesized by glycine nitrate process, Ceram. Int. 35 (1) (2009) 13-20.
- [70] K.A. Berry, M.P. Harmer, Effect of magnesia solute on microstructure development in alumina, J. Am. Ceram. Soc. 69 (2) (1986) 143-149.
- [71] R. Voytovych, I. MacLaren, M.A. Gülgün, R.M. Cannon, M. Rühle, The effect of yttrium on densification and grain growth in α -alumina, Acta Mater. 50 (13) (2002) 3453-3463.
- [72] G. Bernard-Granger, C. Guizard, New relationships between relative density and grain size during solid-state sintering of ceramic powders, Acta Mater. 56 (20) (2008) 6273-6282.
- [73] S.I. Bae, S. Baik, Sintering and grain growth of ultrapure alumina, J. Mater. Sci. 28 (15) (1993) 4197-4204.
- [74] R.L. Coble, Sintering Crystalline Solids. II. Experimental Test of Diffusion Models in Powder Compacts, J. Appl. Phys. 32 (5) (1961) 793-799.
- [75] M.D. Drahus, H.M. Chan, J.M. Rickman, M.P. Harmer, Densification and Grain Growth of FÖ Doped and Fe/Y Codoped Alumina: effect of Fe Valency, J. Am. Ceram. Soc. 88 (2005) 3369-3373.
- [76] J. Fang, A.M. Thompson, M.P. Harmer, H.M. Chan, Effect of Yttrium and Lanthanum on the Final-Stage Sintering Behavior of Ultrahigh-Purity Alumina, J. Am. Ceram. Soc. 80 (2005) 2005-2012.

- [77] Z.R. Hesabi, M. Haghighatzadeh, M. Mazaheri, D. Galusek, S.K. Sadrnezhaad, Suppression of grain growth in sub-micrometer alumina via two-step sintering method, J. Eur. Ceram. Soc. 29 (2009) 1371–1377.
- [78] P.J. Jorgensen, J.H. Westbrook, Role of Solute Segregation at Grain Boundaries During Final Stage Sintering of Alumina, J. Am. Ceram. Soc. 47 (1964) 332-
- [79] L.C. Lim, P.M. Wong, M. Jan, Microstructural evolution during sintering of nearmonosized agglomerate-free submicron alumina powder compacts, Acta Mater. 48 (9) (2000) 2263-2275.
- [80] L. Radonjić, V. Srdić, Effect of magnesia on the densification behavior and grain growth of nucleated gel alumina, Mater. Chem. Phys. 47 (1) (1997) 78-
- [81] S. Sumita, Influence of oxide additives, firing temperature, and dispersing media on sintered Al2O3, J. Ceram. Soc. Jpn. 99 (1151) (1991) 538-544.
- [82] A.M. Thompson, M.P. Harmer, Influence of Atmosphere on the Finaå Stage Sintering Kinetics of Ultrå Higà Purity Alumina, J. Am. Ceram. Soc. 76 (1993) 2248-2256.
- [83] J. Zhao, M.P. Harmer, Sintering of Ultra-High-Purity Alumina Doped Simultaneously with MgO and FeO, J. Am. Ceram. Soc. 70 (12) (1987) 860-866.
- [84] R.M. German, Sintering Simplified: surface Area, Density, and Grain Size Relations, Mater. Sci. Forum 835 (2016) 50-75.
- [85] T.K. Gupta, Sintering of MgO: densification and grain growth, J. Mater. Sci. 6 (1) (1971) 25-32
- [86] X. Li, L. Zhang, Y. Dong, R. Gao, M. Qin, X. Qu, J. Li, Pressureless two-step sintering of ultrafine-grained tungsten, Acta Mater. 186 (2020) 116-123.
- R.P. Rusin, Sintering of Nickel With and Without Dispersed Alumina Particles, Northwestern University, 1993.
- R.M. German, Grain growth influences on the sintering densification of fcc. metals; the example of palladium, Mater. Sci. Res. 13 (1980) 159-166 (Sintering Processes).